The RNA demethylase FTO is required for maintenance of bone mass and functions to protect osteoblasts from genotoxic damage

Qian Zhang[a], Ryan C. Riddle[a,b], Qian Yang[a], Clifford R. Rosen[c], Denis C. Guttridge[d], Naomi Dirckx[a], Marie-Claude Faugere[e], Charles R. Farber[f], and Thomas L. Clemens[a,b,1]

[a]Department of Orthopaedic Surgery, The Johns Hopkins University, Baltimore, MD 21287; [b]Baltimore Veterans Administration Medical Center, Baltimore, MD 21201; [c]Center for Molecular Medicine, Maine Medical Center Research Institute, Scarborough, ME 04074; [d]Department of Pediatrics, Medical University of South Carolina, Charleston, SC 29425; [e]Department of Medicine, University of Kentucky, Lexington, KY 40506; and [f]Center for Public Health Genomics, University of Virginia, Charlottesville, VA 22908

Edited by Brendan H. Lee, Baylor College of Medicine, Houston, TX, and accepted by Editorial Board Member David J. Mangelsdorf July 26, 2019 (received for review April 10, 2019)

The fat mass and obesity-associated gene (*FTO*) encodes an m6A RNA demethylase that controls mRNA processing and has been linked to both obesity and bone mineral density in humans by genome-wide association studies. To examine the role of *FTO* in bone, we characterized the phenotype of mice lacking *Fto* globally (Fto^{KO}) or selectively in osteoblasts ($Fto^{Oc\ KO}$). Both mouse models developed age-related reductions in bone volume in both the trabecular and cortical compartments. RNA profiling in osteoblasts following acute disruption of *Fto* revealed changes in transcripts of *Hspa1a* and other genes in the DNA repair pathway containing consensus m6A motifs required for demethylation by *Fto*. *Fto* KO osteoblasts were more susceptible to genotoxic agents (UV and H_2O_2) and exhibited increased rates of apoptosis. Importantly, forced expression of *Hspa1a* or inhibition of NF-κB signaling normalized the DNA damage and apoptotic rates in *Fto* KO osteoblasts. Furthermore, increased metabolic stress induced in mice by feeding a high-fat diet induced greater DNA damage in osteoblast of $Fto^{Oc\ KO}$ mice compared to controls. These data suggest that FTO functions intrinsically in osteoblasts through Hspa1a–NF-κB signaling to enhance the stability of mRNA of proteins that function to protect cells from genotoxic damage.

bone | osteoblasts | osteoporosis | DNA damage | epigenetics

Osteoporosis, characterized by decreased bone mineral density (BMD) and increased risk of fracture, continues to impact global health with an alarming financial and social burden (1). Like other complex disorders, such as diabetes and obesity, the development of osteoporosis is strongly influenced by genetic factors (2). Large-scale genome-wide association studies (GWAS) have identified numerous loci harboring genetic variants robustly associated with BMD (3, 4). The observation that some of these loci are also associated with obesity and body mass index (3, 5) suggests the existence of common heritable pathways controlling these related physical traits.

The fat mass and obesity-associated gene (*FTO*) was among the first genes to be linked by GWAS to obesity and body composition in multiple human populations (6–8). Subsequently, several SNPs within the *FTO* locus have also been linked to BMD (5). *Fto* was originally described in the fused toe mouse mutant, which carries a 1.6-Mb deletion on chromosome 8 containing 6 separate genes, including *Fto* (9). FTO is a member of the Fe-II and 2-oxygluterate–dependent dioxygenase family (10, 11) and catalyzes the oxidative demethylation of N6-methyladenosine (m6A) in nuclear RNA (12), to influence mRNA splicing, export, localization, translation, and stability (13).

The importance of FTO as a determinant of mammalian growth is suggested by the finding of severe growth retardation and early lethality in individuals carrying a homozygous 947G-A transition in the *FTO* gene (14). However, the major sites of action and mechanism for this RNA-modifying enzyme are still unclear. The current understanding of how FTO controls growth and body composition has been largely inferred from the phenotype in mice lacking *Fto* globally, which exhibit reduced survival rates with postnatal growth retardation, reduced food intake, and reduced adipose tissue (15, 16). Subsequent studies have indicated that FTO influences early differentiation (17) and clonal expansion of adipocyte precursors (18) and alters adipocyte triglyceride metabolism (19). Conversely, unrestricted overexpression of *Fto* caused obesity in mice (20). While such data support a role for FTO in body composition, the precise mechanism by which FTO influences postnatal growth and BMD remains elusive.

In this study, we used genetic mouse models to demonstrate that osteoblast expression of *Fto* is required for normal bone formation in mature mice. Our studies suggest that the bone-preserving actions of FTO are exerted via a cell-autonomous mechanism, which stabilizes endoplasmic reticulum (ER) stress pathway components, such as Hsp70, that normally protect osteoblasts from genotoxicity and cell death.

Results

FTO Is Expressed in Osteoblasts and Is Required for Maintenance of Bone Mass. As a first step in defining the role of FTO in bone, we compared the relative expression of *Fto* mRNA across mouse

Significance

Like other complex disorders, such as diabetes and obesity, osteoporosis is strongly influenced by genetic factors. In this study, we explored the function of the fat mass and obesity-associated gene (FTO), an RNA demethyase that has been strongly linked by genome-wide association studies to obesity and bone density. We show that loss of *Fto* in mouse osteoblasts leads to age-related bone loss with increased susceptibility of osteoblasts to cell death. RNA profiling of osteoblasts lacking *Fto* prioritized FTO targets that are members of the DNA repair pathway, which are activated in response to genotoxic stimuli. Our results identify an epigenetic pathway in which FTO normally functions in bone to enhance the stability of mRNA-encoding proteins that protect osteoblasts from genotoxic damage.

Author contributions: Q.Z. and T.L.C. designed research; Q.Z., Q.Y., C.R.R., N.D., M.-C.F., and C.R.F. performed research; D.C.G. contributed new reagents/analytic tools; Q.Z. and C.R.F. analyzed data; and Q.Z., R.C.R., and T.L.C. wrote the paper.

The authors declare no conflict of interest.

This article is a PNAS Direct Submission. B.H.L. is a guest editor invited by the Editorial Board.

[1]To whom correspondence may be addressed. Email: tclemen5@jhmi.edu.

This article contains supporting information online at www.pnas.org/lookup/suppl/doi:10.1073/pnas.1905489116/-/DCSupplemental.

Published online August 21, 2019.

tissues. *Fto* mRNA was expressed at highest levels in white adipose tissue and specific regions of the brain, including the hippocampus, hypothalamus, and cortex. Moderate levels of *Fto* expression were detected in bone marrow, the femur, and calvaria bones (Fig. 1*A*), whereas expression was low in the heart and skeletal muscle. We next created new strains of mice, which lacked *Fto* globally (Fto^{KO}) or selectively in osteoblasts ($Fto^{Oc\ KO}$), and compared their phenotypes. Immunoblots performed on tissues from the KO mice indicated complete loss of FTO protein in global (Fto^{KO}) mice (*SI Appendix*, Fig. S1*A*), and a marked reduction in *Fto* expression in bone samples from $Fto^{Oc\ KO}$ (*SI Appendix*, Fig. S1*B*). We attribute residual expression of *Fto* in bone from $Fto^{Oc\ KO}$ mice to the contamination from nonosteoblast tissue and not to a partial or incomplete excision of the *Fto* gene.

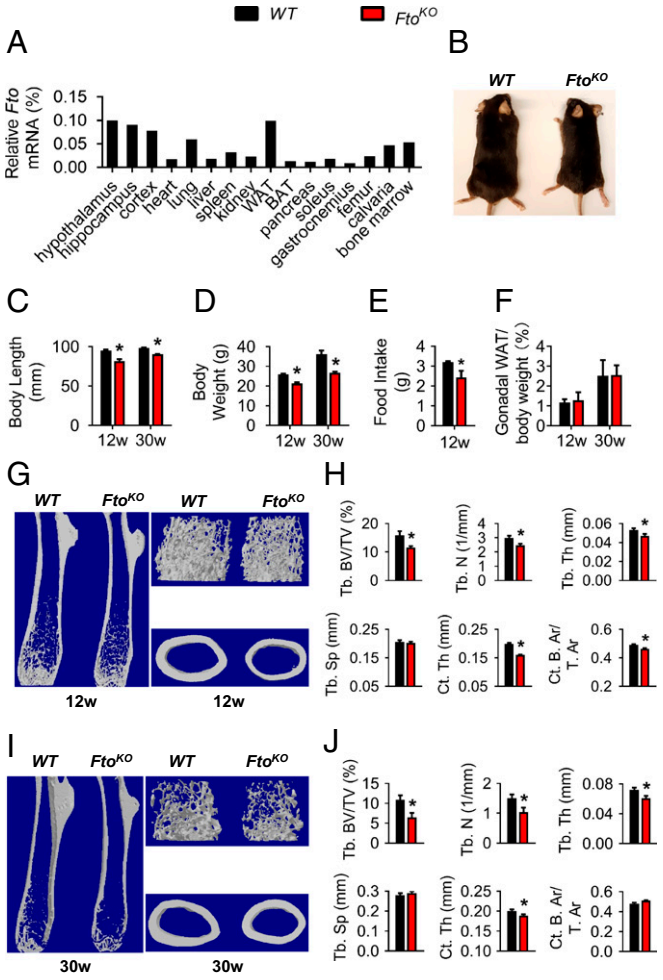

Fig. 1. Unrestricted loss of *Fto* in mice reduces postnatal growth and bone acquisition. (*A*) *Fto* mRNA expression across mouse tissues. (*B*) Representative photograph of a Fto^{KO} mouse and a WT control littermate at 30 wk of age. (*C*) Body length and (*D*) body weight at 12 wk and 30 wk. (*E*) Food intake and (*F*) gonadal fat mass from control and Fto^{KO} mice. (*G*) Representative computer renderings of bone structure in the femurs from control and Fto^{KO} mice at 12 wk. (*H*) Quantitative analysis of femoral trabecular and cortical bone at 12 wk (male, $n = 5$ to 6): Bone volume/tissue volume, BV/TV (%); trabecular number, Tb. N (1/mm); trabecular thickness, Tb. Th (mm); trabecular separation, Tb. Sp (mm); cortical thickness, Ct. Th (mm); bone area/total cross-sectional tissue area, B. Ar/T. Ar. (*I*) Representative computer renderings of bone structure in the femurs from control and Fto^{KO} mice at 30 wk. (*J*) Quantitative analysis of femoral trabecular and cortical bone at 30 wk (male, $n = 5$). $^*P < 0.05$. All error bars represent SEM.

Consistent with published findings (15), global loss of *Fto* in mice resulted in normal litter sizes at birth but ~50% of the offspring of both sexes died within a few days after birth. Analysis of the surviving mice revealed reduced body length (Fig. 1 *B* and *C*) and body weight (Fig. 1*D*) compared with WT littermates at both 12 wk and 30 wk of age. Food intake was also reduced in the Fto^{KO}, but adipose tissue was unaffected when normalized to body weight (Fig. 1 *E* and *F*).

Skeletal morphometry assessed by micro-CT at the femur revealed a loss of both cortical and trabecular bone volume in Fto^{KO} mice. Compared with WT mice, bone volume and tissue volume in the mutants was decreased 30% at 12 wk (Fig. 1*H*) and 40% at 30 wk (Fig. 1*J*), with corresponding reductions in trabecular number and thickness. At the femoral middiaphysis, cortical thickness and bone area/total cross-sectional tissue area (Fig. 1 *H* and *J*) were significantly reduced. In addition, for Fto^{KO} mice at 12 vs. 30 wk we found that while trabecular bone decreases, cortical bone is actually increased during this interval. This apparent compartment-specific alteration may relate in part to the growing of overall body length in the Fto^{KO} mice over this period. Analogous changes in trabecular structure were observed at the spine (*SI Appendix*, Fig. S2).

To assess the impact of Fto on bone mass without potential confounding effects of generalized alterations in body composition on skeletal acquisition, we created mice lacking *Fto* selectively in osteoblasts ($Fto^{Oc\ KO}$). In contrast to the growth and metabolic changes observed in the global Fto^{KO} mice, $Fto^{Oc\ KO}$ mice had no discernable changes in overall growth body weight and length (Fig. 2 *A*–*D*) up to 30 wk of age. In addition, these mice showed no alterations in food intake, body composition (lean and fat mass), or glucose metabolism (*SI Appendix*, Fig. S3). Bone volume in $Fto^{Oc\ KO}$ mice was comparable to controls at 12 wk of age (Fig. 2 *E* and *F*), but was decreased at 30 wk of age (Fig. 2 *G* and *H*), as was trabecular number, (Fig. 2*H*), and increases in trabecular separation (Fig. 2*H*). Measures of cortical bone volume including cortical thickness and bone area/total cross-sectional tissue area were also significantly decreased in mutant mice. Similar but more modest changes were observed at the spine (*SI Appendix*, Fig. S4). Taken together, these data suggest that the early defects in bone volume evident in the global Fto^{KO} mice are due, at least in part, to changes in body composition and metabolism, whereas bone changes in the 30-wk-old $Fto^{Oc\ KO}$ mice are cell autonomous.

Static and dynamic histomorphometric analyses performed at 30 wk of age showed that the decrease in bone volume in $Fto^{Oc\ KO}$ mice was secondary to a reduction of bone formation. Although the numbers of osteoblasts per bone perimeter were similar to controls, the bone formation rate in mutant mice were decreased by 66% at 30 wk old compared to controls (Fig. 2*I* and *SI Appendix*, Table S1). Interestingly, bone marrow adipocyte number per bone marrow area was increased in $Fto^{Oc\ KO}$ mice (Fig. 2*I*), a finding confirmed by CT visualization in osmium tetroxide-fixed femurs (Fig. 2*J*). Moreover, significantly greater numbers of empty osteocytic lacunae were observed in cortical bone from 30-wk-old $Fto^{Oc\ KO}$ mice compared to their control littermates (Fig. 2*K*). Osteoclast numbers were unchanged in $Fto^{Oc\ KO}$ mice when compared to controls (Fig. 2*I* and *SI Appendix*, Table S1) and serum levels of the bone resorption marker CTX were decreased (Fig. 2*L*). The histomorphometry results indicate that the decreased bone volume in $Fto^{Oc\ KO}$ mice is due primarily to a decrease in activity or loss of resident osteoblasts/osteocytes. This ultimately leads to a state of low bone turnover and accumulation of marrow fat, a phenotype compatible with age-related bone loss.

FTO Is Required for Osteoblast Survival and Differentiation. We next determined the requirement for FTO for differentiation and survival of osteoblasts using primary cell cultures. In WT osteoblasts, *Fto* mRNA was expressed at low levels in freshly plated

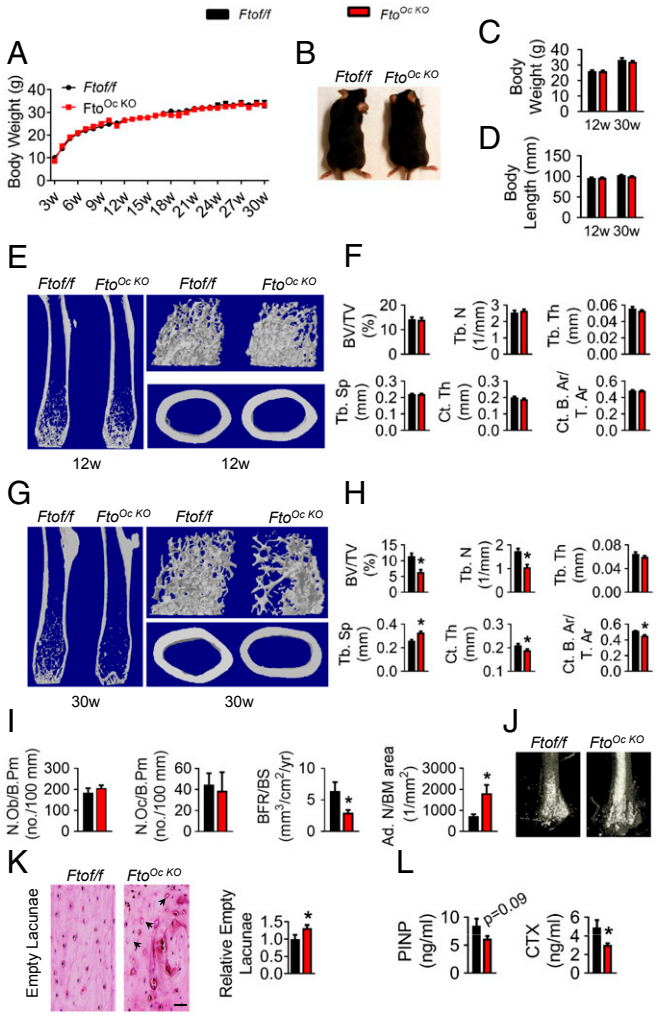

Fig. 2. Mice lacking *Fto* in osteoblasts exhibit normal growth but lose bone with age. (*A*) Growth curves for $Fto^{Oc\ KO}$ and control mice over 30 wk. (*B*) Representative photograph of 30-wk-old $Fto^{Oc\ KO}$ mouse and a control littermate indicating similar body size. (*C*) Body weight and (*D*) body length at 12 wk and 30 wk. (*E*) Representative computer renderings of bone structure in the femurs from *Ftof/f* and $Fto^{Oc\ KO}$ mice at 12 wk (male, $n = 6$ to 8). (*F*) Quantitative analysis of femoral trabecular and cortical bone at 12 wk. (*G*) Representative computer renderings of bone structure in the femurs from *Ftof/f* and $Fto^{Oc\ KO}$ mice at 30 wk (male, $n = 5$ to 7). (*H*) Quantitative analysis of femoral trabecular and cortical bone at 30 wk. (*I*) Histomorphometric analysis of *Ftof/f* and $Fto^{Oc\ KO}$ femur at 30 wk: Osteoblast numbers per bone perimeter, N. Ob/B.Pm; osteoclast numbers per bone perimeter, N. Oc/B. Pm; bone formation rate, BFR/BS; Adipocyte number per bone marrow area, Ad. N/BM area. (*J*) Distribution of marrow adipose tissue (MAT) in the medullary canal. Three-dimensional reconstruction of osmium-stained tibia: Light gray, bone; white, MAT. (*K*) Empty lacunae (arrow) staining of osteocyte and quantification in the cortical bone of 30-wk-old $Fto^{Oc\ KO}$ or control mice. (Scale bar, 200 μm.) (*L*) Serum P1NP and CTX. $^*P < 0.05$. All error bars represent SEM.

cultures and increased by 2-fold over 21 d of in vitro differentiation (Fig. 3*A*). Cre-mediated knockdown of *Fto* in calvarial osteoblasts isolated from mice carrying floxed *Fto* alleles did not significantly alter proliferative capacity as measured by BrdU incorporation at 3 d of culture (Fig. 3*C*). However, loss of *Fto* in osteoblasts showed increased apoptosis assessed by TUNEL (Fig. 3*D*) and caspase cleavage (Fig. 3*E*), and reduced accumulation of mineral (Alizarin) by 21 d of culture (Fig. 3*B*). These changes were accompanied by decreased expression of osteocalcin (Fig. 3*F*). These findings suggest that FTO is required for survival of osteoblasts during differentiation.

The accumulation of marrow fat in mature mice lacking *Fto* in osteoblasts suggested the possibility that FTO might function in mesenchymal cell lineage allocation. To test this idea, we performed colony formation assays (CFU) in marrow harvested from both global Fto^{KO} and $Fto^{Oc\ KO}$ mice. As shown in Fig. 3*G*, the numbers of clonogenic fibroblast colony-forming cells (CFU-F) cultured from marrow of 12-wk-old Fto^{KO} mice was markedly reduced compared to cells from WT mice and formed fewer CFU-osteoblasts (Ob) when cultured in osteoblast differentiation medium (Fig. 3*H*). The marrow from the Fto^{KO} mice formed fewer numbers of Oil-red O^+ colonies when cultured in adipocyte differentiation medium (Fig. 3*I*). These findings are compatible with previous studies, which reported that FTO is required in early mesenchymal expansion and adipocyte differentiation (17). Similar changes in CFU-F and CFU-Ob were observed in marrow cultures from $Fto^{Oc\ KO}$ mice (Fig. 3 *J* and *K*). Oil-red O colonies were increased (Fig. 3*L*) when differentiated in osteoblast and adipocyte medium, respectively. Similar changes were observed in marrow cultures from 30-wk-old mice (Fig. 3 *J*–*L*). These findings indicate that loss of *Fto* in osteoblast lineage cells compromises their early differentiation and survival.

Loss of *Fto* in Osteoblasts Increases Susceptibility to Genotoxic Damage. To identify possible downstream targets of FTO in osteoblasts, we profiled global RNA transcripts by RNA sequencing (RNA-seq) in primary mouse osteoblasts following Cre-mediated disruption of *Fto*. A total of 45 transcripts were significantly (false-discovery rate < 0.05) differently expressed as a function of *Fto* disruption when compared to controls at 24 h (Dataset S1). Pathway analysis indicated major alterations in transcripts encoded by genes known to function in the genotoxic damage response (gene ontology term "DNA Repair", $P = 0.002$) (*SI Appendix*, Table S2), including members of the heat-shock family (e.g., *Hspa1a* encoding Hsp70). We focused on DNA repair for 2 reasons. First, "DNA repair" was identified as a significantly altered pathway after *Fto* knockdown ($P_{adj} = 2.7 \times 10^{-3}$) and this pathway has previously been linked to FTO (21). Second, individual gene members of the DNA repair pathway, *Kdm2a* and *Hspa1a*, were 2 of the top 3 most significant perturbed genes (false-discovery rate < 1.5×10^{-9}) (Dataset S1).

DNA damage following exposure to genotoxic agents is known to activate the ER stress response pathway triggering heat-shock proteins, which in turn, engage immune signaling networks to initiate apoptosis of damage cells (22). To explore a possible role for FTO in the genotoxic damage, we compared the susceptibility of WT and *Fto* KO osteoblasts to 2 well-established genotoxic agents, UV light and H_2O_2. Osteoblasts lacking *Fto* were more susceptible to UV-induced damage as indicated by greater γH2AX immunoreactivity (Fig. 4*A*). Similarly, treatment of primary osteoblasts from $Fto^{Oc\ KO}$ mice with H_2O_2 resulted in greater DNA damage (Fig. 4 *B* and *C*) and increased rates of apoptosis as indicated by increased numbers of annexin V^+ cells and cleaved caspase 3 levels (Fig. 4 *D* and *E*) as compared to control cells. Comet assays showed no tail DNA in $Fto^{Oc\ KO}$ and WT primary osteoblasts prior to inducing genotoxic stress, suggesting that *Fto* deletion per se does not cause DNA damage (Fig. 4*C*). In contrast, deletion of *Fto* significantly increased tail DNA in osteoblasts exposed to H_2O_2 (Fig. 4*C*). Consistent with the notion that *Fto* protects osteoblasts from DNA damage, γH2AX immunoreactivity was observed in a greater proportion of osteocalcin-positive cells of marrow derived from 30-wk-old $Fto^{Oc\ KO}$ mice compared to controls (Fig. 4*F*). In addition, loss of *Fto* greatly increased the percentages of tail DNA (comet assay) in bone marrow-derived stem cells (BMSCs) derived from 30-wk-old mice (Fig. 4*G*). Moreover, γH2AX immunoreactivity was present in a greater proportion of osteoblasts (Fig. 4*H*) and osteocytes (Fig. 4*I*) from $Fto^{Oc\ KO}$ mice femur compared to control (*Ftof/f*) mice.

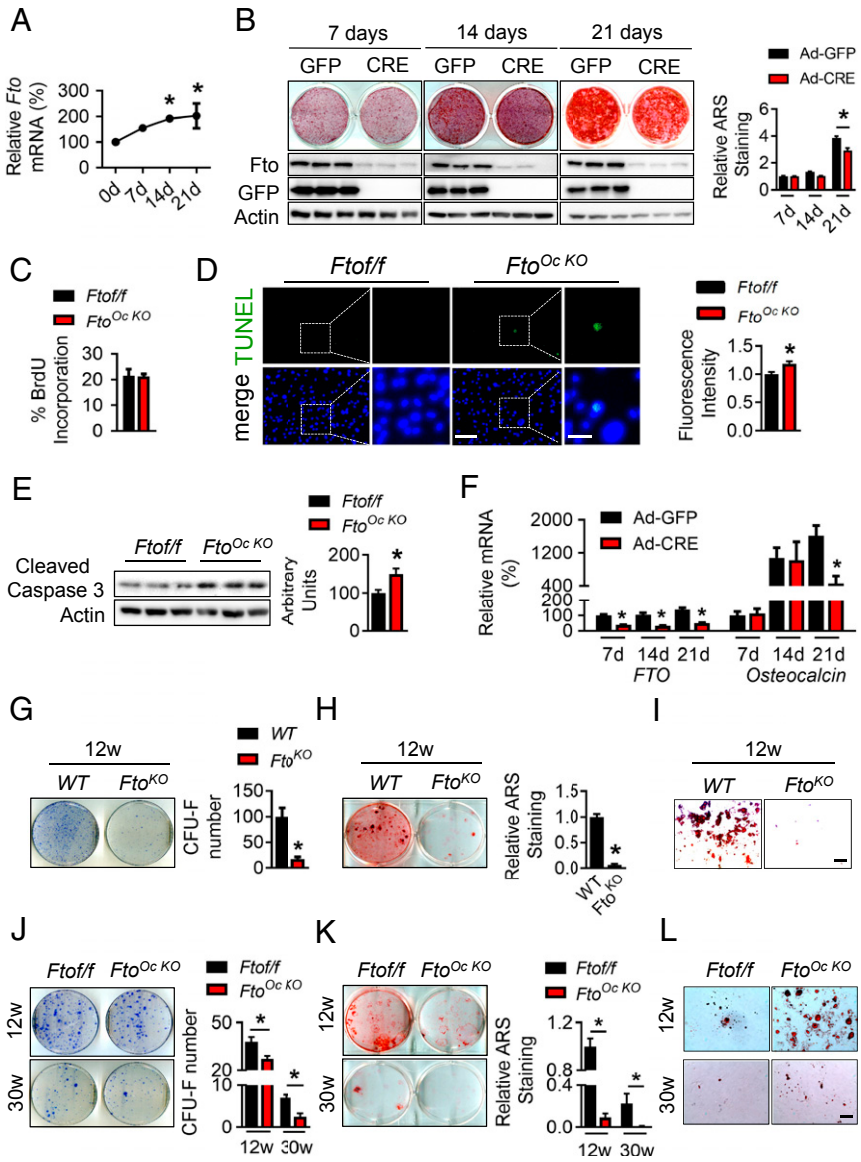

Fig. 3. Loss of *Fto* in vitro impairs osteoblast differentiation. (*A*) *Fto* mRNA levels in 0-, 7-, 14-, 21-d differentiated primary osteoblasts ($n = 3$). (*B*) Examination of osteoblast differentiation after the deletion of *Fto* by Alizarin red (ARS) staining after 7, 14, and 21 d of differentiation, with FTO and GFP expression, respectively. Relative ARS levels ($n = 6$) was quantified. (*C*) Quantification of osteoblast proliferation by BrdU uptake in primary osteoblasts isolated from control and $Fto^{Oc\ KO}$ mice ($n = 3$). (*D*) TUNEL staining of primary osteoblasts at 21 d of differentiation. The images are representative of 4 wells. (Scale bars: *Left,* 500 μm; *Right,* 200 μm.) (*E*) Immunoblot of cleaved caspase 3 in $Fto^{Oc\ KO}$ cells differentiated for 14 d. (*F*) RT-PCR analysis of *Fto* and osteocalcin expression after osteoblasts differentiation ($n = 3$). (*G–L*) BMSC were isolated from bone marrow, cultured in complete medium, or osteogenic induction medium, or adipogenic induction medium. (*G*) CFU-F and quantification ($n = 3$); (*H*) CFU-Ob and quantification ($n = 3$); and (*I*) CFU-Ad ($n = 3$) in BMSC from 12 wk old *Fto* global KO mice. (Scale bar: 200 μm.) (*J*) CFU-F ($n = 4$ to 6); (*K*) CFU-Ob ($n = 6$); and (*L*) CFU-Ad ($n = 4$) in BMSC from 12- and 30-wk-old male $Fto^{Oc\ KO}$ mice. (Scale bar: 200 μm.) $^*P < 0.05$. All error bars represent SEM.

FTO Targets Multiple Proteins in the Genotoxic Damage/ER Stress-Response Pathway. To validate *Fto* targets, we determined the impact of loss of *Fto* on the expression of down-regulated transcripts from the RNA profile (*SI Appendix*, Table S2) associated with DNA repair, including *Hspa1a* (23), *Cdk9* (24), *Kdm2a* (25), and *Ube2v1* (26), each of which contained the predicted m6A motif (27) (*SI Appendix*, Fig. S5*A*). Disruption of *Fto* in primary osteoblasts decreased the expression of each of these transcripts (Fig. 5*A*). RT-PCR of RNA following a methylated RNA immunoprecipitation (MeRIP) with an m6A-specific antibody (28, 29), showed enrichment in *Hspa1a* and *Ube2v1* mRNA in the *Fto* KO osteoblasts as compared to controls (Fig. 5*B*). Consistent with the in vitro result, *Hspa1a* mRNA expression in femora from 30-wk-old $Fto^{Oc\ KO}$ mice was also down-regulated (Fig. 5*C*).

We prioritized Hsp70 for further study because of its established role in the ER stress pathway, where it is known to block activation of NF-κB via stabilization of the inhibitory complex with inhibitor of NF-κB (IκB) (30, 31). Consistent with this concept, p-p65 levels were increased in *Fto* KO osteoblasts compared to controls (Fig. 5*D*). Moreover, forced expression of Hspa1a in the *Fto* KO osteoblasts inhibited the increase of p-p65–NF-κB (*SI Appendix*, Fig. S5 *A* and *B*) and prevented the increase of γH2AX seen with *Fto* KO alone in both UV-treated primary osteoblasts (*SI Appendix*, Fig. S5*C*) and BMSC from 30-wk-old mice (*SI Appendix*, Fig. S5*E*). Comet assay showed that overexpression in *Hspa1a*-attenuated DNA damage in *Fto* deleted cells under the stimulation of UV (*SI Appendix*, Fig. S5*D*). Taken together, these results indicate that Hspa1a and NF-κB are linked downstream

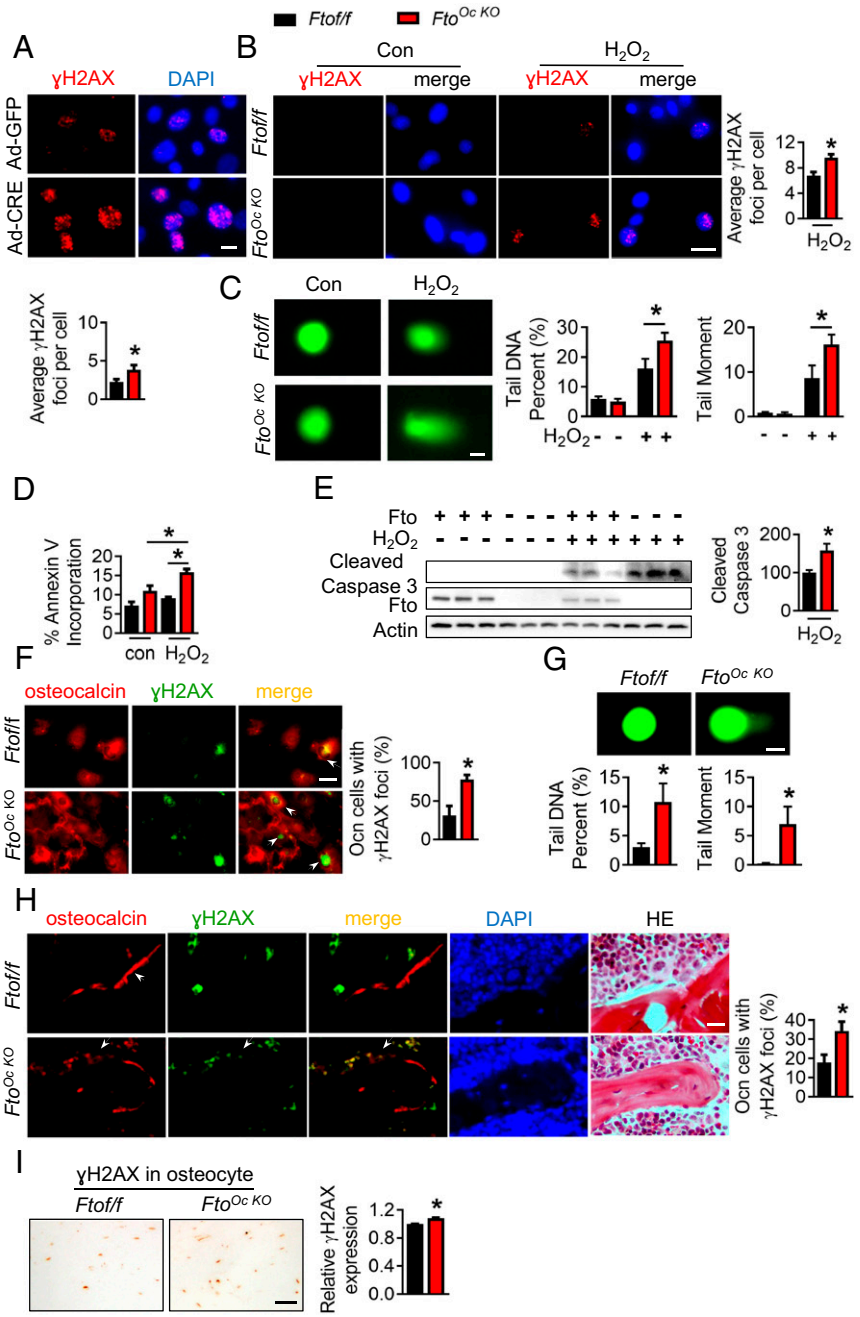

Fig. 4. *Fto* loss increases susceptibility if osteoblasts to genotoxic stimuli. (*A*) Primary *Ftof/f* osteoblasts were infected with a Cre-expressing or control adenovirus, then subjected to 2′ 15J UV-C irradiation, and stained for γH2AX. About 50 cells were analyzed in each group. (Scale bar, 50 μm.) (*B*) After H_2O_2 incubated for 6 h, γH2AX was stained in the primary osteoblasts derived from $Fto^{Oc\ KO}$ or control pups ($n = 3$ to 4). Approximately 70 to 90 cells were counted in each group. (Scale bar: 100 μm.) (*C*) Representative images and quantification of comet assay of Fto^{+} or Fto^{-} cells at 6 h after H_2O_2 treatment. Quantification was summarized data from 40 to 80 cells in each group. (Scale bar: 25 μm.) (*D*) Annexin V assays and (*E*) cleaved caspase 3 expression after 6-h incubation of H_2O_2 in primary osteoblasts. (*F*) BMSC from 30-wk-old $Fto^{Oc\ KO}$ or control mice costained for osteocalcin and γH2AX. White arrows indicate colocalization of γH2AX and osteocalcin. About 50 to 100 cells were counted in the quantification. (Scale bar: 200 μm.) (*G*) Representative images of comet assay show that deletion of *Fto* increased in DNA damage in BMSCs from 30-wk-old mice. Quantification of 35 to 50 cells was in each group. (Scale bar: 50 μm.) (*H*) Femur from 30-wk-old $Fto^{Oc\ KO}$ or control mice costained for osteocalcin and γH2AX. White arrows indicate osteocalcin (red), γH2AX (green) or colocalization of γH2AX and osteocalcin (yellow); 100 to 200 cells were counted in each group. (Scale bar: 100 μm.) (*I*) γH2AX staining of osteocyte in the cortical bone of 30-wk-old $Fto^{Oc\ KO}$ or control mice. (Scale bar: 50 μm.) $^{*}P < 0.05$. All error bars represent SEM.

targets of FTO. Moreover, treatment of primary osteoblasts with an NF-κB inhibitor MLN-120B, largely restored the defective mineralization and increased apoptosis of *Fto*-null osteoblasts (Fig. 5 *E* and *F*).

To determine whether pharmacologic suppression of NF-κB signaling in vivo also results in recovery of DNA damage, a peptide inhibitor of IKK, termed the NEMO-binding domain (NBD), was used (32–35). The activity of the peptide was first verified in vitro by demonstrating a reduction in nuclear p-p65 in primary osteoblasts (*SI Appendix*, Fig. S5*F*). Next, 29-wk-old $Fto^{Oc\ KO}$ mice were treated with NBD (10 mg/kg, i.p., every other day) for 10 d, and bone was harvested for analysis of DNA damage. As

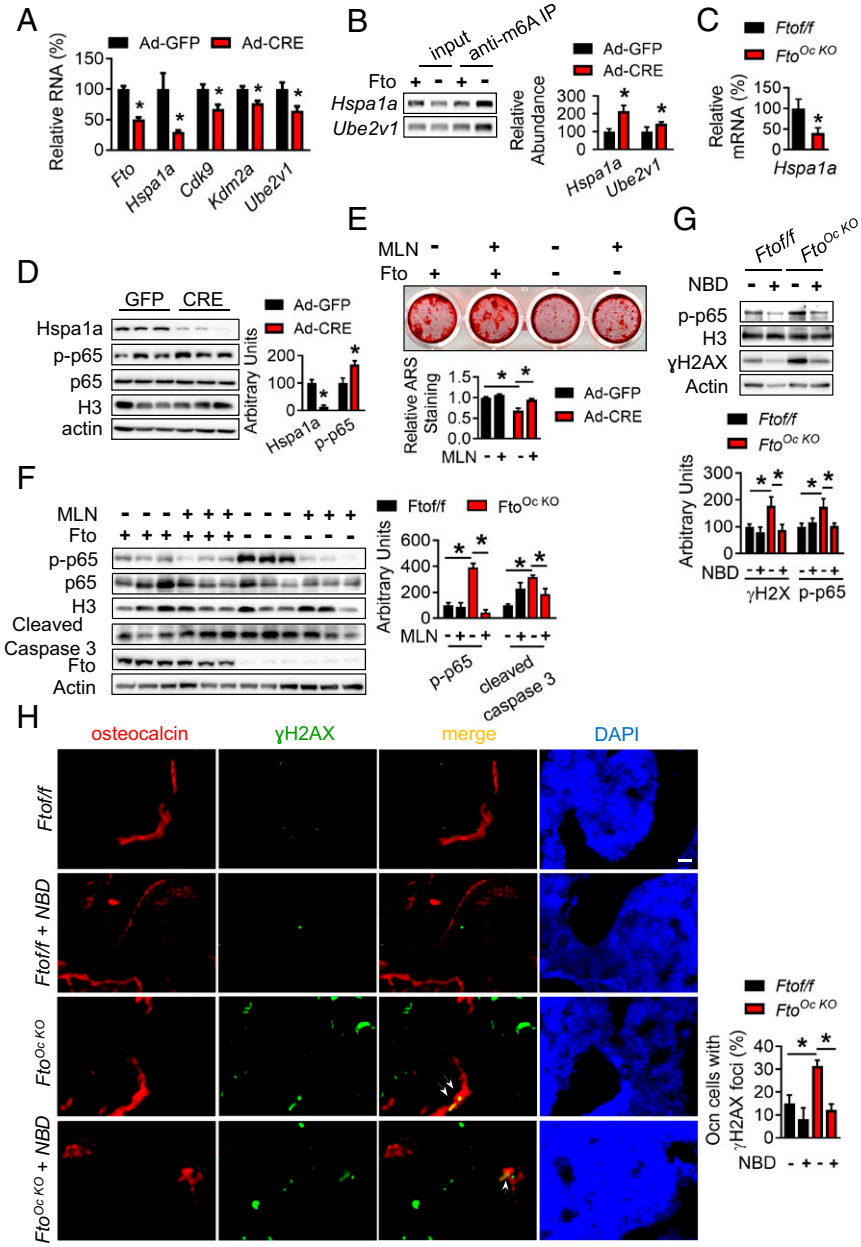

Fig. 5. FTO modulates osteoblast apoptosis through the Hspa1a–NF-κB pathway. (*A*) mRNA expression in primary osteoblasts with 24-h inhibition of *Fto* by adenovirus ($n = 3$). (*B*) Effect of *Fto* KO on m6A-methylation of *Hspa1a* and *Ube2v1* from mRNA in primary osteoblasts after m6A-specific MeRIP. mRNA abundance was determined by RT-PCR and calculated relative to the input sample ($n = 3$). (*C*) RT-PCR of *Hspa1a* expression in femur from 30-wk-old $Fto^{Oc\ KO}$ and *Ftof/f* mice ($n = 5$ to 6). (*D*) Immunoblot of Hspa1a and p-p65 NF-κB after 24 h of *Fto* deletion in primary osteoblasts. (*E* and *F*) Fourteen-day differentiated control and $Fto^{Oc\ KO}$ osteoblasts were treated with 10 μM MLN-120B for 7 d, ARS staining (*E*) and Western blot of relative protein expression (*F*) were performed with quantifications ($n = 3$). After injection of NBD in $Fto^{Oc\ KO}$ and *Ftof/f* mice, (*G*) immunoblot of γH2AX in femur (male, $n = 4$ to 5) and (*H*) immunofluoresence staining of femur bone sections were detected. White arrows indicate colocalization of γH2AX and osteocalcin (yellow). (Scale bar: 100 μm.) $^*P < 0.05$. All error bars represent SEM.

shown in Fig. 5 *G* and *H*, NBD administration attenuated γH2AX immunoreactivity in osteoblasts from $Fto^{Oc\ KO}$ mice compared to controls (*Ftof/f*).

Osteoblasts Lacking *Fto* Are More Susceptible to Genotoxic Damage Induced by Metabolic Stress. The increased susceptibility to DNA damage in *Fto* KO osteoblasts exposed to H_2O_2 (Fig. 4) suggested that FTO might protect cells from genotoxic damage associated with generalized metabolic stress. Previous studies have shown that excessive accumulation of lipids, referred to lipotoxicity, activates the ER stress pathway in a number of cell/tissue types (36). We therefore examined the role of FTO in standard experimental models of lipotoxicity. In primary osteoblasts cultured in the presence of the saturated fatty acids stearate or palmitate, DNA damage and apoptotic rates were more pronounced in osteoblasts lacking *Fto* compared to controls (Fig. 6 *A*–*F*).

To assess the impact of loss of FTO function in a pathophysiological setting of lipotoxicity in vivo, 6-wk-old male $Fto^{Oc\ KO}$ and control littermates were fed a chow or standard high-fat (HF) diet for 12 wk, then killed, and their bone cells examined for evidence of DNA damage. HF diet feeding increased total body

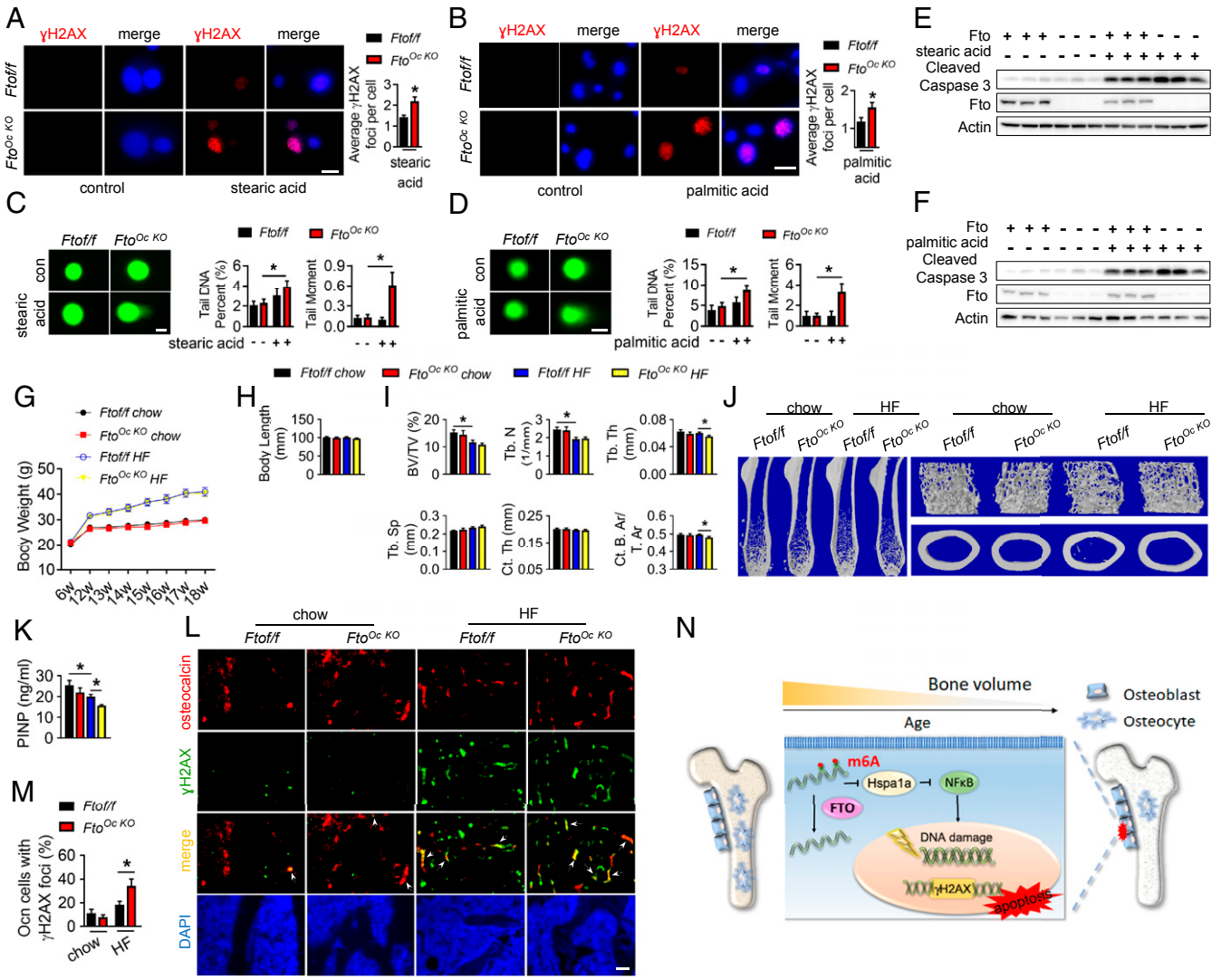

Fig. 6. Loss of *Fto* exacerbates osteoblast DNA damage in mice fed a HF diet. (*A* and *B*) γH2AX staining in *Fto*$^{+}$ or *Fto*$^{-}$ primary osteoblasts after stearic acid (*A*) or palmitic acid (*B*) incubation overnight; 100 to 150 cells were counted in each group. (Scale bars: 200 μm.) (*C* and *D*) Comet assays in primary osteoblasts after stearic acid (*C*) or palmitic acid (*D*) incubation overnight; 20 to 50 cells in each group were used for quantification. (Scale bars: 100 μm.) (*E* and *F*) Cleaved caspase 3 levels were detected in primary osteoblasts after stearic acid (*E*) or palmitic acid (*F*) incubation overnight. (*G*–*K*) Six-week-old male mice were fed chow or HF diets for 12 wk and the analysis was performed at 18 wk of age (chow diet, $n = 6$ to 7; HF diet, $n = 17$ to 19). (*G*) Growth curve of *Fto*$^{Oc\ KO}$ and control mice from 6 to 18 wk. (*H*) Body length of HF-diet mouse at 18 wk old. (*I*) Quantitative analysis of femoral trabecular and cortical bone at 18 wk. (*J*) Representative computer renderings of bone structure in the femurs from HF-fed *Ftof/f* and *Fto*$^{Oc\ KO}$ mice at 18 wk. (*K*) Serum P1NP. (*L* and *M*) Femur from 18-wk-old HF-*Fto*$^{Oc\ KO}$ or control mice were costained for osteocalcin and γH2AX and quantified. White arrows indicate colocalization of γH2AX and osteocalcin (yellow). (Scale bar: 200 μm.) (*N*) Proposed model FTO function in bone (see text for details). *$P < 0.05$. All error bars represent SEM.

weight to a similar degree in both *Fto*$^{Oc\ KO}$ and control *(Ftof/f)* mice (Fig. 6 *G* and *H*), but reduced trabecular thickness and cortical bone area in the mutants relative to controls (Fig. 6 *I* and *J*). HF feeding was also associated with lower serum P1NP levels in *Fto*$^{Oc\ KO}$ compared to *Ftof/f* mice (Fig. 6*K*). DNA damage as assessed by γH2AX in osteoblasts of the femurs from *Fto*$^{Oc\ KO}$ mice was significantly greater in mutant mice fed the HF diet compared with controls (Fig. 6 *L* and *M*). These findings further support the notion that FTO protects osteoblasts from genotoxic stress.

Discussion

In this study, we characterized the role of the RNA demethylase FTO in bone using genetic models designed to avoid the potentially confounding effects of FTO on global metabolism and body composition. Our results show that osteoblast expression of *Fto* acts in a cell-autonomous fashion to protect osteoblasts from genotoxic-induced apoptosis and thereby preserves bone mass.

Previous studies in mouse models lacking *Fto* globally have reported alterations in postnatal growth and skeletal acquisition but with several significant phenotypic differences. For example, Fischer et al. (15) reported that global deletion of *Fto* in mice leads to high embryonic lethality, postnatal growth retardation, and a significant reduction in adipose tissue and lean body mass. In contrast, Church et al. (37) found that mice carrying a point mutation, which eliminated the demethylase catalytic activity, had reduced fat mass, increased energy expenditure, and unchanged physical activity. However, when *Fto* was selectively deleted in adipocytes, mature mice demonstrated increased fat mass due to impaired lipolysis and accelerated triglyceride clearance through modulation of Angptl4 (19). While previous studies and the data presented here suggest that global loss of *Fto* is associated with

reduced bone volume (16, 38), interpretation of these findings is complicated due to the potential for confounding effects of changes in overall growth, body size, and body composition.

To more precisely define the role of FTO in bone, we created both global and osteoblast-specific *Fto* KO models and compared their phenotypes. A side-by-side comparison of both models revealed reductions in bone mass that strongly support an osteoblast intrinsic role for FTO in preserving bone formation during adulthood. This conclusion is supported by several additional lines of evidence. First, *Fto* was expressed at relatively high levels in osteoblasts of WT mice. Second, osteoblast precursors lacking *Fto* differentiated poorly and demonstrated increased rates of apoptosis. Moreover, loss of *Fto* in osteoblast lineage cells reduced the ability of mesenchymal colonies to form osteoblasts (CFU-Ob) while increasing the numbers of adipocyte precursors. Finally and most importantly, the decreased trabecular bone in mice lacking *Fto* was associated with decreased bone formation by resident osteoblasts and fewer surviving osteocytes. These results indicate that FTO is required for the maintenance of osteoblast lineage cell precursors and their subsequent ability to differentiate and form bone. These alterations in mouse bone are compatible with the skeletal changes associated with age-related bone loss in humans, including a decline in the rate of bone formation and an increase in bone marrow adiposity (39–42).

Given our in vitro data showing that FTO is required for limiting osteoblast death from DNA damage, we might have expected to see fewer osteoblasts in the bones from the KO mice. The lack of a significant decrease in osteoblast numbers in vivo may simply be due to the relatively small numbers of total osteoblasts measured at the femoral trabecular bone compartment in older mice. Unfortunately, the apoptotic rate of these cells, which we would anticipate to be elevated, cannot be accurately quantified due to the low percentage (<1%) of apoptosis in normal osteoblasts (43). In this regard, the increased empty osteocytic lacunae observed in $Fto^{Oc\ KO}$ bones is certainly compatible with an increased apoptotic rate of osteocytes, and by inference, osteoblasts. Clearly, the finding of reduced bone formation rates per bone surface is suggestive of a defect in osteoblast function, possibly as a consequence of accumulation of DNA damage and incipient apoptosis. It is highly unlikely that osteoclast numbers or activity explain the reduced bone volume in $Fto^{Oc\ KO}$ mice since total numbers of osteoclasts per bone perimeter were unchanged (i.e., not increased) and serum Ctx was reduced.

Our focus on the DNA damage/stress pathway as a potential site for FTO action in osteoblasts was based on unbiased RNA profiling, which disclosed alterations in the expression of transcripts with the predicted m6A consensus motif for FTO binding. Key among these is the chaperone Hsp70, which is known to play a central role in the ER stress response (44–46). Programmed cell death triggered by the accumulation of DNA damage is a common phenomenon in many cell types. In this pathway, the induction of Hsp70 induced in response to both intrinsic and extrinsic stressors protects cells from apoptosis in part by inhibiting the expression of NF-κB (47, 48). In agreement with this concept, *Fto* KO osteoblasts were more susceptible to apoptosis in response to experimental genotoxic damage. Moreover, reexpression of Hsp70 or inhibition of in NF-κB signaling in *Fto* KO cells ameliorated their sensitivity to genotoxicity and apoptosis.

We fully recognize the possibility that the bone changes observed in mice lacking *Fto* here might have resulted in part through FTO targets aside from those associated with DNA damage. Indeed, some of the transcripts altered in cells lacking *Fto* did not contain the consensus sequence, suggesting that they might represent secondary or downstream events possibly in compensation for the loss of *Fto*. Importantly, however, FTO functions in bone do not appear to involve IRX3 or IRX5, previously reported to influence aditpocyte lineage (49), since these transcripts were unchanged in the *Fto*-null cells (*SI Appendix*, Fig. S6).

With these caveats in mind, it is reasonable to conclude that FTO represents an important epigenetic mechanism that functions in bone to protect osteoblasts from genotoxic damage through stabilization of components of the ER stress pathway (Fig. 6*N*). Such a mechanism would enable FTO to regulate the expression of multiple components of the stress response, simultaneously protecting cells from apoptosis when exposed to genotoxic damage. In this regard, it is important to note that NF-κB signaling is increased in bone from aged mice and genetic depletion of the p65 can protect osteoblasts from reactive oxygen species-associated DNA damage and retard age-related bone loss (50, 51). Our finding that loss of *Fto* also increased susceptibility of osteoblasts to genotoxic damage from metabolic stress induced by exposure to HF is also consistent with this model for FTO action. We believe that these findings in mice are relevant to human bone and may account at least in part for the strong linkage of this gene with BMD.

Methods

Mice and Treatment Protocols. All procedures involving mice were approved by the Institutional Animal Care and Use Committee of The Johns Hopkins University. *Fto* flox/flox (*Ftof/f*) mice, in which exon 3 is flanked by loxP sites and when excised results in a frameshift causing early termination in translation, were a gift from Pumin Zhang, Department of Biochemistry and Molecular Biology, Baylor College of Medicine, Houston, TX (16). Mice lacking *Fto* in osteoblasts ($Fto^{Oc\ KO}$) were generated by crossing osteocalcin-Cre (Oc-Cre) transgenic mice (52) with *Ftof/f* mice. To generate global KO mice, *Ftof/f* mice were crossed with the ubiquitous Cre delete strain B6.C-Tg (CMV-Cre) 1Cgn/J (The Jackson Laboratory), generating homozygous knockout mice (Fto^{KO}). Fto^{KO} mice were backcrossed to WT C57BL/6 mice to remove Cre and bred to homozygosity. Results are reported for male mice on the same genetic background (C57BL6/J). For the diet-induced bone loss studies, mice were fed a 60% high-fat diet (D12492, Research Diets) from 6 wk of age to 24 wk. Genotyping strategies are available upon request. NBD (KKKKKKKKGGTALDWSWLQTE) with the Trp to Ala substitutions designed to render the peptide inactive underlined, was a gift from D.C.G. and dissolved in water before use. Next, 10 mg/kg NBD was intraperitoneally injected in 29-wk old $Fto^{Oc\ KO}$ mice every other day for 9 d. One day after the last injection, bone was harvested for analysis of DNA damage.

Primary Cells Isolation and Culture. Osteoblasts were isolated from calvaria of newborn mice by serial digestion in 1.8 mg/mL of collagenase. For in vitro analysis, osteoblasts were isolated from *Ftof/f* and $Fto^{Oc\ KO}$ mice; alternatively, osteoblasts isolated from *Ftof/f* mice were infected with adenovirus-encoding Cre recombinase or green fluorescent protein (Vector Biolabs), as previously described (53). Infection with 100 mulitiplicity of infection was used in all experiments. Osteoblast differentiation was induced by supplementing α-MEM media with 10% FBS, 10 mM b-glycerol phosphate, and 50 μg/mL ascorbic acid. Alkaline phosphatase and Alizarin red S staining were carried out according to standard techniques. For DNA damage analysis, cells were treated for 200 μM H_2O_2. For the forced Hspa1a expression, pcDNA5/FRT/TO HIS HSPA1A (#19537, Addgene) was a gift from Harm Kampinga, Department of Cell Biology, University Medical Center Groningen, University of Groningen, Groningen, The Netherlands (54), and the control plasmid vector was pcDNA5/FRT/TO vector. The plasmids were transfected using Lipofectamine 3000 Transfection Reagent (L3000008, Thermo Fisher Scientific) following their protocol. To mimic the high-fat feeding in vitro, cells were incubated with 200 μM stearate (Sigma-Aldrich) or 200 μM palmitate (Sigma-Aldrich). Stearate was resuspended in ethanol and heated at 65 °C to fully dissolve, then conjugated to BSA by a 1:20 dilution in a 10% BSA PBS solution and heated at 65 °C for 15 min to make a stearate solution. For palmitate solution, a 20 mM solution of fatty acid in 0.01 M NaOH was incubated at 70 °C for 30 min. Dropwise addition of 1 N NaOH facilitated solubilization of the fatty acid. Fatty acid soaps were complexed with 5% fatty acid-free BSA in PBS at an 8:1 fatty acid to BSA molar ratio.

Bone marrow was isolated from *Ftof/f*, $Fto^{Oc\ KO}$, Fto^{KO} and WT littermate mice, as previously described (55). To generate BMSC, marrow cells were washed and resuspended in complete media and incubated overnight. Adherent cells were collected as BMSC, and cell purity was confirmed >95% negative for nonspecific esterase (a marker for cells of the monocyte/macrophage lineage).

For assay of CFU-F, BMSC were plated in triplicate over a range of plating densities in a 10-cm dish in complete growth medium composing α-MEM (Invitrogen) supplemented with 10% FBS (Corning), sodium pyruvate (1 mM), and glutamin (2 mM). Culture medium were changed every 3 d. On day 14,

cells were briefly rinsed with PBS and fixed with 4% PFA for 10 min, then stained with 1 mg/mL Methylene blue in Borate buffer (10 mM, pH 8.8) for 30 min. For CFU-Ob assay, established colonies were stimulated for 14 d by osteogenic induction medium: α-MEM supplemented with 10% FBS, 10 nM dexamethasone, 10 mM b-glycerol phosphate, and 50 μg/mL ascorbic acid. At the end of mineralization period, cells were fixed in ethanol and stained with 40 mM Alizarin red solution for calcium deposition. For the CFU-adipocyte (CFU-Ad) assay, cells were seeded in 6-well plates in triplicate and treated with adipogenic induction media (DMEM containing 10% FBS, 1 μM dexamethasone, 200 μM indomethacin, 10 μg/mL insulin, and 0.5 mM methylisobutylxanthine) for 2 d, followed by a 9-d incubation in maintenance media (DMEM with 10% FBS plus 10 μg/mL insulin) with media replaced every 3 d. For Oil-red O staining, the cells were washed, fixed, and stained with Oil-red O solution. Oil-red O solution was freshly prepared by diluting a stock solution (0.5 g of Oil-red O in 100 mL of isopropanol) with water (6:4) followed by filtration.

RNA Preparation and RNA-Seq Analysis. Total RNA was extracted using TriZol, reverse transcribed using iScript cDNA Synthesis Kit (Bio-Rad), and amplified by real-time PCR using SYBR GREEN PCR Master Mix (Bio-Rad). β-Actin was used as housekeeping gene. Primer sequences were from PrimerBank (https://pga.mgh.harvard.edu/primerbank/index.html). For the RNA-seq experiment, after fragment analysis, RNA was sent and subsequently analyzed at the Core Facility at University of Virginia.

m6A MeRIP. Total osteoblast RNA was subjected to RiboMinus kit (Invitrogen) to deplete rRNA following the manufacturer's instruction, and then fragmented with Ambion RNA Fragmentation Reagent (Invitrogen). m6A immunoprecipitation (IP) was carried out with rabbit polyclonal anti-m6A antibody (Synaptic Systems, 202003) using protocols described previously (28, 56). In brief, fragmented RNA was immunoprecipitated in 300 μL of IP buffer (10 mM Na phosphate, 0.05% Triton-X, 140 mM NaCl) with 300 μL of anti-m6A antibody-coupled Dynabeads (Invitrogen) for 2 h at 4 °C. Beads were then washed in 500 μL of 1× IP buffer 5 times, and the supernatant saved for the sake of IP quality control. To elute m6A-enriched RNA fragments from the beads, 200 μL of elution buffer (5 mM Tris·HCl, pH 7.5, 1 mM EDTA, 0.05% SDS and 2.8 μL proteinase K [20 mg/mL]) was added to the beads and incubated at 50 °C for 1.5 h, with shaking every 15 min. The beads were washed once with 100 μL elution buffer and the supernatant collected. Combined eluates were then treated with 0.1 volume of 3 M sodium acetate (pH 5.2), and 2.5 volumes of prechilled ethanol to isolate eluted RNA. cDNA was generated from input and eluted RNA samples using iScript cDNA Synthesis Kit (Bio-Rad). RT-PCR was performed and calculated relative to the input sample with *Gusb* (a nonm6A-containing mRNA) used as endogenous control.

Immunoblot Analysis. To extract protein from long bones, the attached muscles and tissues were removed, the epiphyseal ends were cut, and the marrow was flushed out; then the bone was grinded with liquid nitrogen in the presence of proteinase inhibitor and phosphatase inhibitor. Immediately after grinding, we transfered the ground femur to a microfuge tube containing lysis buffer. For cell samples, total protein was extracted using RIPA lysis buffer, and nuclear protein was extracted using protocol from Rockland antibodies and assays. Immunoblot was performed according to standard techniques. Primary antibodies anti-FTO (1:1,000, #597-FTO, PhosphoSolutions), anti-γH2AX (1:1,000, ab26350, Abcam), anti-Hspa1a (1:1,000, C92F3A-5, Enzo Life Sciences), anti-p–NF-κB p65 (1:1,000, 3033S, Cell Signaling Technology), anti-t–NF-κB p65 (1:1,000, 4764S, Cell Signaling Technology), anticleaved-caspase-3 (1:1,000, 9664S, Cell Signaling Technology), and anti–β-actin (1:1,000, 3700S, Cell Signaling Technology) were incubated overnight at 4 °C.

Immunostaining. Paraffin sections of bone were deparaffinized at 60 °C for 20 min. Sections were then treated with 100% xylene for 5 min twice, 100% ethanol for 5 min, 95% ethanol for 3 min, and 70% ethanol for 3 min and rinsed with PBS for 1 min twice, followed by antigen retrieval with citrate buffer (DAKO) at 90 °C for 30 min. Blocking was done with Protein Block Reagent (DAKO). Anti-γH2AX (1:500, ab26350, Abcam) and antiosteocalcin (1:500, Sc-30044, Santa Cruz) antibodies were used. Secondary staining was done with goat anti-rabbit AF594 (1:1,000, Invitrogen) and goat anti-mouse AF488 (1:1,000, Invitrogen) or goat anti-mouse AF594 (1:1,000, Invitrogen). The nuclei were counter stained with DAPI and images were obtained using a fluorescence microscope (IX71 Olympus). γH2AX fluorescence per cell was quantified using ImageJ software. This was normalized by comparing the quantified blue signal of the same cells imaged for DAPI staining.

Comet Assay. Cells were analyzed with Trevigen Comet Assay kit (4250-050-K) under alkaline conditions. Images were taken with an Olympus fluorescence microscope with a similar background. Using a comet assay plugin from ImageJ that allows a mathematical calculation of DNA contents in the head and tail of a comet, DNA damage was quantified as the percentage of tail DNA and tail moment.

Osmium Tetroxide Staining. To assess marrow adipose tissue, mouse bones were infiltrated with osmium tetroxide as described previously (57). Briefly, bones were fixed in 4% PFA and decalcified in 14% EDTA, pH 7.4, for 14 d. After washing with water, we cut off the tibia just proximal to the ankle joint and incubated the bone in 1% osmium tetroxide in the fume hood for 48 h. After being washed, all of the waste contaminated by osmium tetroxide was disposed properly, the bones were removed from the fume hood, and scanned in micro-CT with energy of 55 kV.

TUNEL Staining and Flow Cytometry. Osteoblast proliferation was assessed by flow cytometry with a BrdU kit (559619, BD Pharmingen). Briefly, control and Fto^{KO} osteoblasts were cultured in α-MEM containing 10% FBS. At 30% confluence, BrdU (10 μM) was added to the medium for 16 h before harvesting the cells. Cells were stained with anti-BrdU-FITC and 7-aminoactinomycin D (7AAD) and assessed by LSR II (BD Biosciences). H_2O_2 induced apoptotic cells were detected using an Annexin V antibody (563544, BD Biosciences), and assessed by LSR II. Ten-thousand events were collected for each sample and the results analyzed by FlowJo 7.6. TUNEL staining was performed by in situ cell ceath detection kit (Roche Applied Science).

Imaging and Histomorphometry. Mice were killed at the indicated age and bone volume in the distal femoral metaphysis was assessed using a desktop microtomographic imaging system (Skyscan 1275). For the trabecular bone analysis, a region of interest (ROI) was selected and delineated into 2-mm segments along the longitudinal direction. The vertical distance between the first image in the ROI and the growth plate was 0.5 mm. For the cortical bone analysis, from the midpoint of the femur, 0.25 mm toward the proximal end, and 0.25 mm toward the distal end, represented the ROI. Histological analyses, using a semiautomatic method (Osteoplan II, Kontron) were carried out on 30-wk-old mice injected with 1% calcein (wt/vol) at 8 and 3 d before sacrifice. Histomorphometric parameters follow the recommended nomenclature of the American Society of Bone and Mineral Research (58). Body composition was measured by QNMR (EchoMRI-100).

Statistical Analysis. All data are expressed as means ± SEM. Significant differences were assessed using unpaired, 2-tailed Student *t* test or 1-way ANOVA followed by the Student–Newman–Keuls test. $P < 0.05$ was considered statistically significant.

ACKNOWLEDGMENTS. We thank Dr. Pumin Zhang for providing the *Ftof/f* mouse model. This work was supported by VA Merit Review Grant BX001234 (to T.L.C.) and NIH Grant DK099134 (to R.C.R.). T.L.C. also receives support from a Senior Research Career Scientist Award from the Department of Veterans Affairs. M.-C.F. is supported by the Kentucky Nephrology Research Fund.

1. N. Harvey, E. Dennison, C. Cooper, Osteoporosis: Impact on health and economics. *Nat. Rev. Rheumatol.* **6**, 99–105 (2010).
2. A. Battle, C. D. Brown, B. E. Engelhardt, S. B. Montgomery; GTEx Consortium; Laboratory, Data Analysis &Coordinating Center (LDACC)—Analysis Working Group; Statistical Methods groups—Analysis Working Group; Enhancing GTEx (eGTEx) groups; NIH Common Fund; NIH/NCI; NIH/NHGRI; NIH/NIMH; NIH/NIDA; Biospecimen Collection Source Site—NDRI; Biospecimen Collection Source Site—RPCI; Biospecimen Core Resource—VARI; Brain Bank Repository—University of Miami Brain Endowment Bank; Leidos Biomedical—Project Management; ELSI Study; Genome Browser Data Integration &Visualization—EBI; Genome Browser Data Integration &Visualization—UCSC Genomics Institute, University of California Santa Cruz; Lead analysts; Laboratory, Data Analysis &Coordinating Center (LDACC); NIH program management; Biospecimen collection; Pathology; eQTL manuscript working group, Genetic effects on gene expression across human tissues. *Nature* **550**, 204–213 (2017).
3. G. M. Calabrese, *et al*., Integrating GWAS and Co-expression network data identifies bone mineral density genes SPTBN1 and MARK3 and an osteoblast functional module. *Cell Syst.* **4**, 46–59.e4 (2017).
4. J. P. Kemp *et al*., Identification of 153 new loci associated with heel bone mineral density and functional involvement of GPC6 in osteoporosis. *Nat. Genet.* **49**, 1468–1475 (2017).
5. Y. Guo *et al*., The fat mass and obesity associated gene, FTO, is also associated with osteoporosis phenotypes. *PLoS One* **6**, e27312 (2011).

6. A. Scuteri *et al.*, Genome-wide association scan shows genetic variants in the FTO gene are associated with obesity-related traits. *PLoS Genet.* **3**, e115 (2007).
7. T. M. Frayling *et al.*, A common variant in the FTO gene is associated with body mass index and predisposes to childhood and adult obesity. *Science* **316**, 889–894 (2007).
8. C. Dina *et al.*, Variation in FTO contributes to childhood obesity and severe adult obesity. *Nat. Genet.* **39**, 724–726 (2007).
9. T. Peters, K. Ausmeier, U. Ruther, Cloning of Fatso (Fto), a novel gene deleted by the Fused toes (Ft) mouse mutation. *Mamm. Genome* **10**, 983–986 (1999).
10. L. Sanchez-Pulido, M. A. Andrade-Navarro, The FTO (fat mass and obesity associated) gene codes for a novel member of the non-heme dioxygenase superfamily. *BMC Biochem.* **8**, 23 (2007).
11. T. Gerken *et al.*, The obesity-associated FTO gene encodes a 2-oxoglutarate-dependent nucleic acid demethylase. *Science* **318**, 1469–1472 (2007).
12. G. Jia *et al.*, N6-methyladenosine in nuclear RNA is a major substrate of the obesity-associated FTO. *Nat. Chem. Biol.* **7**, 885–887 (2011).
13. Y. Fu, D. Dominissini, G. Rechavi, C. He, Gene expression regulation mediated through reversible m^6A RNA methylation. *Nat. Rev. Genet.* **15**, 293–306 (2014).
14. S. Boissel *et al.*, Loss-of-function mutation in the dioxygenase-encoding FTO gene causes severe growth retardation and multiple malformations. *Am. J. Hum. Genet.* **85**, 106–111 (2009).
15. J. Fischer *et al.*, Inactivation of the Fto gene protects from obesity. *Nature* **458**, 894–898 (2009).
16. X. Gao *et al.*, The fat mass and obesity associated gene FTO functions in the brain to regulate postnatal growth in mice. *PLoS One* **5**, e14005 (2010).
17. M. Zhang *et al.*, The demethylase activity of FTO (fat mass and obesity associated protein) is required for preadipocyte differentiation. *PLoS One* **10**, e0133788 (2015).
18. M. Merkestein *et al.*, FTO influences adipogenesis by regulating mitotic clonal expansion. *Nat. Commun.* **6**, 6792 (2015).
19. C. Y. Wang *et al.*, Loss of FTO in adipose tissue decreases Angptl4 translation and alters triglyceride metabolism. *Sci. Signal.* **8**, ra127 (2015).
20. C. Church *et al.*, Overexpression of Fto leads to increased food intake and results in obesity. *Nat. Genet.* **42**, 1086–1092 (2010).
21. Y. Xiang *et al.*, RNA m^6A methylation regulates the ultraviolet-induced DNA damage response. *Nature* **543**, 573–576 (2017).
22. W. P. Roos, B. Kaina, DNA damage-induced cell death by apoptosis. *Trends Mol. Med.* **12**, 440–450 (2006).
23. P. Niu *et al.*, Overexpressed heat shock protein 70 protects cells against DNA damage caused by ultraviolet C in a dose-dependent manner. *Cell Stress Chaperones* **11**, 162–169 (2006).
24. K. Storch, N. Cordes, The impact of CDK9 on radiosensitivity, DNA damage repair and cell cycling of HNSCC cancer cells. *Int. J. Oncol.* **48**, 191–198 (2016).
25. L. L. Cao *et al.*, ATM-mediated KDM2A phosphorylation is required for the DNA damage repair. *Oncogene* **35**, 301–313 (2016).
26. H. D. Ulrich, H. Walden, Ubiquitin signalling in DNA replication and repair. *Nat. Rev. Mol. Cell Biol.* **11**, 479–489 (2010).
27. Y. Zhou, P. Zeng, Y. H. Li, Z. Zhang, Q. Cui, SRAMP: Prediction of mammalian N6-methyladenosine (m6A) sites based on sequence-derived features. *Nucleic Acids Res.* **44**, e91 (2016).
28. K. D. Meyer *et al.*, Comprehensive analysis of mRNA methylation reveals enrichment in 3′ UTRs and near stop codons. *Cell* **149**, 1635–1646 (2012).
29. J. Yu *et al.*, Dynamic m6A modification regulates local translation of mRNA in axons. *Nucleic Acids Res.* **46**, 1412–1423 (2018).
30. R. G. Giffard, R. Q. Han, J. F. Emery, M. Duan, J. F. Pittet, Regulation of apoptotic and inflammatory cell signaling in cerebral ischemia: The complex roles of heat shock protein 70. *Anesthesiology* **109**, 339–348 (2008).
31. M. Y. Sherman, V. L. Gabai, Hsp70 in cancer: Back to the future. *Oncogene* **34**, 4153–4161 (2015).
32. M. J. May *et al.*, Selective inhibition of NF-kappaB activation by a peptide that blocks the interaction of NEMO with the IkappaB kinase complex. *Science* **289**, 1550–1554 (2000).
33. S. Acharyya *et al.*, Interplay of IKK/NF-kappaB signaling in macrophages and myofibers promotes muscle degeneration in Duchenne muscular dystrophy. *J. Clin. Invest.* **117**, 889–901 (2007).
34. A. Ghosh *et al.*, Selective inhibition of NF-kappaB activation prevents dopaminergic neuronal loss in a mouse model of Parkinson's disease. *Proc. Natl. Acad. Sci. U.S.A.* **104**, 18754–18759 (2007).
35. D. Friedmann-Morvinski *et al.*, Targeting NF-κB in glioblastoma: A therapeutic approach. *Sci. Adv.* **2**, e1501292 (2016).
36. J. Han, R. J. Kaufman, The role of ER stress in lipid metabolism and lipotoxicity. *J. Lipid Res.* **57**, 1329–1338 (2016).
37. C. Church *et al.*, A mouse model for the metabolic effects of the human fat mass and obesity associated FTO gene. *PLoS Genet.* **5**, e1000599 (2009).
38. G. Sachse *et al.*, FTO demethylase activity is essential for normal bone growth and bone mineralization in mice. *Biochim. Biophys. Acta Mol. Basis Dis.* **1864**, 843–850 (2018).
39. O. Demontiero, C. Vidal, G. Duque, Aging and bone loss: New insights for the clinician. *Ther. Adv. Musculoskelet. Dis.* **4**, 61–76 (2012).
40. M. Almeida *et al.*, Skeletal involution by age-associated oxidative stress and its acceleration by loss of sex steroids. *J. Biol. Chem.* **282**, 27285–27297 (2007).
41. P. Meunier, J. Aaron, C. Edouard, G. Vignon, Osteoporosis and the replacement of cell populations of the marrow by adipose tissue. A quantitative study of 84 iliac bone biopsies. *Clin. Orthop. Relat. Res.* **80**, 147–154 (1971).
42. E. J. Moerman, K. Teng, D. A. Lipschitz, B. Lecka-Czernik, Aging activates adipogenic and suppresses osteogenic programs in mesenchymal marrow stroma/stem cells: The role of PPAR-gamma2 transcription factor and TGF-beta/BMP signaling pathways. *Aging Cell* **3**, 379–389 (2004).
43. R. L. Jilka, R. S. Weinstein, T. Bellido, A. M. Parfitt, S. C. Manolagas, Osteoblast programmed cell death (apoptosis): Modulation by growth factors and cytokines. *J. Bone Miner. Res.* **13**, 793–802 (1998).
44. M. Daugaard, M. Rohde, M. Jäättelä, The heat shock protein 70 family: Highly homologous proteins with overlapping and distinct functions. *FEBS Lett.* **581**, 3702–3710 (2007).
45. D. D. Mosser *et al.*, The chaperone function of hsp70 is required for protection against stress-induced apoptosis. *Mol. Cell. Biol.* **20**, 7146–7159 (2000).
46. C. Bivik, I. Rosdahl, K. Ollinger, Hsp70 protects against UVB induced apoptosis by preventing release of cathepsins and cytochrome c in human melanocytes. *Carcinogenesis* **28**, 537–544 (2007).
47. R. Ran *et al.*, Hsp70 promotes TNF-mediated apoptosis by binding IKK gamma and impairing NF-kappa B survival signaling. *Genes Dev.* **18**, 1466–1481 (2004).
48. K. J. Park, R. B. Gaynor, Y. T. Kwak, Heat shock protein 27 association with the I kappa B kinase complex regulates tumor necrosis factor alpha-induced NF-kappa B activation. *J. Biol. Chem.* **278**, 35272–35278 (2003).
49. M. Claussnitzer *et al.*, FTO obesity variant circuitry and adipocyte browning in humans. *N. Engl. J. Med.* **373**, 895–907 (2015).
50. B. Yu *et al.*, Wnt4 signaling prevents skeletal aging and inflammation by inhibiting nuclear factor-κB. *Nat. Med.* **20**, 1009–1017 (2014).
51. X. C. Bai *et al.*, Reactive oxygen species stimulates receptor activator of NF-kappaB ligand expression in osteoblast. *J. Biol. Chem.* **280**, 17497–17506 (2005).
52. M. Zhang *et al.*, Osteoblast-specific knockout of the insulin-like growth factor (IGF) receptor gene reveals an essential role of IGF signaling in bone matrix mineralization. *J. Biol. Chem.* **277**, 44005–44012 (2002).
53. K. Fulzele *et al.*, Disruption of the insulin-like growth factor type 1 receptor in osteoblasts enhances insulin signaling and action. *J. Biol. Chem.* **282**, 25649–25658 (2007).
54. J. Hageman, H. H. Kampinga, Computational analysis of the human HSPH/HSPA/DNAJ family and cloning of a human HSPH/HSPA/DNAJ expression library. *Cell Stress Chaperones* **14**, 1–21 (2009).
55. M. Doucet *et al.*, CCL20/CCR6 signaling regulates bone mass accrual in mice. *J. Bone Miner. Res.* **31**, 1381–1390 (2016).
56. D. Dominissini *et al.*, Topology of the human and mouse m6A RNA methylomes revealed by m6A-seq. *Nature* **485**, 201–206 (2012).
57. E. L. Scheller *et al.*, Use of osmium tetroxide staining with microcomputerized tomography to visualize and quantify bone marrow adipose tissue in vivo. *Methods Enzymol.* **537**, 123–139 (2014).
58. D. W. Dempster *et al.*, Standardized nomenclature, symbols, and units for bone histomorphometry: A 2012 update of the report of the ASBMR Histomorphometry Nomenclature Committee. *J. Bone Miner. Res.* **28**, 2–17 (2013).